JOURNAL OF PROPULSION AND POWER
Vol. 18, No. 5, September–October 2002

Nonlinear Heterogeneous Model of Composite Solid-Propellant Combustion

B. Rasmussen* and R. A. Frederick Jr.†
University of Alabama in Huntsville, Huntsville, Alabama 35899

A computational model of composite solid-propellant combustion that combines three important properties is described. First, the model is heterogeneous, in that it incorporates a multilevel flame structure similar to the Beckstead–Derr–Price proposition. Second, it is nonsteady, and its main purpose is to predict pressure-coupled frequency response. Third, it is fully nonlinear, where thermal capacitance calculations come from a computational solution of the transient heat-conduction equation separately in the oxidizer and binder. Calculations show a frequency response that varies significantly with oxidizer particle diameter and mean pressure. Some observed trends are that the magnitude of the real part of R_P tends to diminish with higher mean pressures and that propellants with very coarse oxidizer particles tend to develop two peaks, one for the oxidizer and one for the binder.

Nomenclature

A	=	preexponential factor; unit area
C_p	=	constant pressure specific heat
D	=	oxidizer particle diameter; diffusion coefficient
d	=	thermal diffusivity
E	=	activation energy
f	=	generic function
G	=	mass flux
K	=	turbulent mixing coefficient
M	=	molecular weight
n	=	pressure exponent
P	=	pressure
q	=	specific energy
R_P	=	pressure-coupled frequency response
$\Re$	=	universal gas constant
T	=	temperature
t	=	time
x	=	distance
α	=	mass fraction
β	=	power factor in diffusion coefficent
ζ	=	volumetric fraction
λ	=	thermal conductivity
ν	=	exponential factor
ρ	=	density
σ	=	surface fraction; temperature sensitivity
τ	=	characteristic response time

Subscripts and Superscript

ap	=	ammonium perchlorate
b	=	binder
diff	=	diffusion
f	=	flame
g	=	gas phase
i	=	initial state
k	=	vector subscript
p	=	total propellant; constant pressure
r	=	reaction
ref	=	reference condition
s	=	surface; solid
v	=	vaporization
0	=	reference conditions
$*$	=	characteristic value

Presented as Paper 99-2228 at the AIAA/ASME/SAE/ASEE 35th Joint Propulsion Conference and Exhibit, Los Angeles, CA, 20–23 June 1999; received 7 August 1999; revision received 1 February 2002; accepted for publication 14 June 2002.

*Graduate Research Assistant, UAH Propulsion Research Center, Department of Mechanical and Aerospace Engineering.

†Associate Professor, UAH Propulsion Research Center. Associate Fellow AIAA.

Introduction

THIS paper describes a nonlinear, nonsteady, computational model of composite solid-propellant combustion, similar to the Beckstead–Derr–Price (BDP) 1970 model.[1] Whereas most models in the BDP framework have been steady-state constructions, the present model is an attempt to extend the concept to a nonsteady regime. Specifically, the goal is to predict the nonlinear frequency response of burning rate to pressure oscillations.

Previous research has produced linearized, nonsteady BDP-type models (see Refs. 2 and 3), as well as nonlinear composite models with homogeneous assumptions,[4,5] but the current attempt is both nonlinear and heterogeneous. The basic theoretical picture not as complicated as some of the more refined steady-state models[6] because computational restrictions associated with nonlinear simulation tend to lengthen the list of assumptions.

The model applies to composite propellants with ammonium perchlorate (AP) oxidizers and hydroxyl-terminated polybutadiene (HTPB) binders, although the model could extend directly to other polymer binders by simply changing material and chemical constants in the computation. The model can only simulate propellants with one oxidizer particle diameter, that is, monomodal propellants. In nonsteady simulations, the model only considers thermodynamic effects such as temperature profiles in the solid region and shifting flame heights and temperatures. It does not consider nonsteady chemical changes such as induced oxidizer-to-fuel (O/F) ratio oscillations. It is quasi one dimensional, where two- or three-dimensional effects collapse into "characteristic" values (Fig. 1).

This idealized model differs from real combustion in several significant ways. First, practical propellants are almost always polydisperse. Second, there is no such thing as an absolute flame height or temperature. The model in this paper retracts the flame region into a set of characteristic flame heights and temperatures that define the heat fluxes into the surface. Third, in real composite propellant deflagration, heat moves laterally through fluid flow on the surface and conduction between binder and oxidizer.

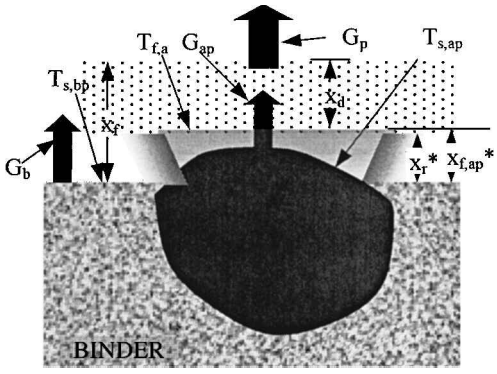

Fig. 1 Idealized Sketch.

Basic Equations

Mass Fluxes

By assumption, the mass fluxes of oxidizer and binder depend solely on their respective surface temperatures through Arrhenius pyrolysis. Some research has indicated that simple Arrhenius pyrolysis may not be a complete description of nonsteady burning, and other relationships, such as the one-step, zeroth-order relation may be a better approximation.[7] The nonsteady portion of the current model, however, does include thermal capacitance in the solid phase, just as the zeroth-order relation does. These effects do not show up directly in the surface pyrolysis relationships, but they do alter the burning rate through manipulation of the surface temperature.

The mass flux of oxidizer and binder are, respectively,

$$G_{\mathrm{ap}} = A_{s,\mathrm{ap}} \exp(-E_{s,\mathrm{ap}}/RT_{s,\mathrm{ap}}) \tag{1}$$

$$G_b = A_{s,b} \exp(-E_{s,b}/RT_{s,b}) \tag{2}$$

The total mass flux derives from a time-averaged combination of the constituent mass fluxes. A line of unit length drawn into the propellant normal to the surface will have a certain fraction of oxidizer and the rest binder. On average, the fraction taken up by oxidizer is the volumetric fraction of oxidizer in the unburned propellant, likewise for the binder. The total linear burning rate is, therefore, $r = 1/(\zeta_{\mathrm{ap}}/r_{\mathrm{ap}} + \zeta_b/r_b)$. Normalizing by density to convert linear burning rate to mass flux, the total mass flux is

$$G_p = 1/\lfloor \alpha_{\mathrm{ap}}/G_{\mathrm{ap}} + (1-\alpha_{\mathrm{ap}})/G_b \rfloor \tag{3}$$

Mass conservation now dictates the relative surface areas that the constituents occupy. The total mass flux leaving the surface is

$$G_{\mathrm{ap}}\sigma_{\mathrm{ap}} + G_b(1-\sigma_{\mathrm{ap}}) = G_p \tag{4}$$

or, solving for σ_{ap},

$$\sigma_{\mathrm{ap}} = (G_p - G_b)/(G_{\mathrm{ap}} - G_b) \tag{5}$$

Equation (5) implies that, when the linear burning rate of the oxidizer is higher than the linear burning rate of the binder, σ_{ap} is smaller than the volumetric fraction of oxidizer (and vice versa).

As a consequence of the change in surface area, the characteristic diameter of a burning AP particle at the surface changes as well. A plane that intersects a packed bed of randomly distributed spheres encounters an average intersection diameter[8] of $D_i(\frac{2}{3})^{1/2}$. Thus, when the linear burning rate of oxidizer is identical to that of the binder, the surface fraction of oxidizer is equal to the volumetric fraction, and the characteristic diameter is just $D_i(\frac{2}{3})^{1/2}$. When the linear burning rates are different, however, the characteristic diameter changes.

The total surface area that the oxidizer occupies is the number of oxidizer particles multiplied by the characteristic particle diameter D^*, that is,

$$\sigma_{\mathrm{ap}} = (\text{number of oxidizer particles}) \cdot (D^*)/(\text{unit length}) \tag{6}$$

When it is assumed that the number of oxidizer particles on the surface remains constant regardless of burning rate, even though their average diameters might change, the relation becomes

$$\sigma_{\mathrm{ap}}/\zeta_{\mathrm{ap}} = D^*/D_i\sqrt{2/3} \qquad \text{or} \qquad D^* = (\sigma_{\mathrm{ap}}/\zeta_{\mathrm{ap}})D_i\sqrt{2/3} \tag{7}$$

Surface Temperatures

Energy balances from deep within the propellant to just above the surface provide surface temperature equations for the oxidizer and binder. There is no term for radiant heat flux, and so the equations only apply to situations where conduction is the dominant means of energy transfer. Energy balances for the oxidizer and binder, respectively, are

$$G_{\mathrm{ap}}C_{p,s,\mathrm{ap}}T_i + \lambda_{g,\mathrm{ap}}\left.\frac{\partial T}{\partial x}\right|_{x=0^+} + G_{\mathrm{ap}}q_{v,\mathrm{ap}} = G_{\mathrm{ap}}C_{p,s,\mathrm{ap}}T_{s,\mathrm{ap}} + \int_{-\infty}^{0} \rho_{s,\mathrm{ap}}C_{p,s,\mathrm{ap}}\frac{\partial T_{\mathrm{ap}}}{\partial t}\partial x \tag{8}$$

$$G_bC_{p,s,b}T_i + \lambda_{g,b}\left.\frac{\partial T}{\partial x}\right|_{x=0^+} + G_bq_{v,b} = G_bC_{p,s,b}T_{s,b} + \int_{-\infty}^{0} \rho_{s,b}C_{p,s,b}\frac{\partial T_b}{\partial t}\partial x \tag{9}$$

where the coordinate system for all space-dependent equations in this paper is a Lagrangian system, with $x = 0$ at the surface and $x = -\infty$ deep within the propellant.

The derivative terms on the left-hand sides of Eqs. (8) and (9) represent heat conducted into the surface, and the integral terms on the right-hand sides represent thermal capacitance in the solid phase. The specific energy q_v represents total energy required to vaporize the substance. Each q_v might include positive terms for exothermic reactions and negative terms for endothermic reactions or latent heats. The model does not directly account for reactions that occur significantly below the surface, although energy from the reactions might be included in the q_v terms. For example, the energy required to force the phase transition in AP from orthorhombic to cubic is included in $q_{v,\mathrm{ap}}$, but the phase transition is assumed to occur at or near the surface. This assumption facilitates calculation of temperature profiles in the nonsteady part of the model.

To calculate the conductive terms in Eqs. (8) and (9), it is necessary to postulate a temperature profile above each surface. It seems reasonable that the temperature profiles in the gas phase would be exponential in shape. Thus, the assumed temperature profiles above the oxidizer and binder are

$$T = T_{f,\mathrm{ap}} - (T_{f,\mathrm{ap}} - T_{s,\mathrm{ap}}) \exp\left(-\nu x \Big/ x^*_{f,\mathrm{ap}}\right) \tag{10}$$

$$T = T_f - (T_f - T_{s,b}) \exp\left(-\nu x \Big/ x^*_f\right) \tag{11}$$

where ν is a constant equal to 2.5. The inclusion of ν forces the temperature to be close to the corresponding flame temperature at the corresponding characteristic flame height.

Equation (11) implies that the flame is relatively homogeneous above the binder. Above the oxidizer, however, the temperature profile has one exponential form in the premixed flame [Eq. (10)] then another exponential form in the diffusion flame [Eq. (15) to be given]. Although the reaction flame does occur directly above the oxidizer/binder interface, it does not directly alter the temperature profiles above either the oxidizer or the binder. It does, of course, alter the system as a whole by changing the position of energy release.

Differentiating Eqs. (10) and (11) with respect to x and substituting the results into Eqs. (8) and (9) gives the following two expressions for $T_{s,\mathrm{ap}}$ and $T_{s,b}$:

$$T_{s,\mathrm{ap}} = \frac{G_{\mathrm{ap}}C_{p,s,\mathrm{ap}}T_i + \left(\lambda_{g,\mathrm{ap}}T_{f,\mathrm{ap}}\nu \big/ x^*_{f,\mathrm{ap}}\right) + G_{\mathrm{ap}}q_{v,\mathrm{ap}}}{G_{\mathrm{ap}}C_{p,s,\mathrm{ap}} + \left(\lambda_{g,\mathrm{ap}}\nu \big/ x^*_{f,\mathrm{ap}}\right)}$$
$$- \int_{-\infty}^{0} \rho_{s,\mathrm{ap}}C_{p,s,\mathrm{ap}}\left(\frac{\partial T_{\mathrm{ap}}}{\partial t}\right)\mathrm{d}x \Bigg/ \left(G_{\mathrm{ap}}C_{p,s,\mathrm{ap}} + \frac{\lambda_{g,\mathrm{ap}}\nu}{x^*_{f,\mathrm{ap}}}\right) \quad (12)$$

$$T_{s,b} = \frac{G_bC_{p,s,b}T_i + \left(\lambda_{g,b}T_f\nu \big/ x^*_f\right) + G_bq_{v,b}}{G_bC_{p,s,b} + \left(\lambda_{g,b}\nu \big/ x^*_f\right)}$$
$$- \int_{-\infty}^{0} \rho_{s,b}C_{p,s,b}\left(\frac{\partial T_b}{\partial t}\right)\mathrm{d}x \Bigg/ \left(G_bC_{p,s,b} + \frac{\lambda_{g,b}\nu}{x^*_f}\right) \quad (13)$$

Note a critical approximation implied here: The energy balances presented do not explicitly account for the fact that a line drawn normal to the surface into the propellant encounters regions of oxidizer and regions of binder. That is, Eqs. (8) and (9) imply that an area of the surface that is binder will continue to be binder "all of the way down," or at least until the temperature profile levels out at T_i. A real temperature profile, in contrast, contains "kinks" as it changes slope moving through regions of binder and oxidizer. Hopefully, errors introduced by this assumption tend to average out over the course of the entire solution, but there is no guarantee that they do so. Future work in this area should include a better statistical model of the interior of the propellant, similar to some of the previous statistical descriptions of the surface.[9]

Characteristic AP Flame Temperature

The characteristic temperature of the premixed flame, $T_{f,\mathrm{ap}}$, is not equal to the adiabatic flame temperature of AP because, quite simply, it is not adiabatic. The final flame temperature T_f is higher than $T_{f,\mathrm{ap}}$ so that heat conducts from the final flame into the premixed flame. On the other end, $T_{s,\mathrm{ap}}$ is lower than $T_{f,\mathrm{ap}}$, so that heat conducts from the premixed flame into the surface. Thus, $T_{f,\mathrm{ap}}$ can be either higher or lower than the adiabatic flame temperature of AP. When the premixed flame is very close to the surface and the final flame is very far away, the $T_{f,\mathrm{ap}}$ will be low. Conversely, when the premixed flame is relatively long and the final flame is relatively short, $T_{f,\mathrm{ap}}$ will be high.

An energy balance from $x^*_{f,\mathrm{ap}}$ to x^*_f provides an equation for $T_{f,\mathrm{ap}}$. In the balance to follow, there is no thermal capacitance term because the flame is quasi steady by assumption. The balance is

$$G_pC_{p,g,p}T_{f,\mathrm{ap}} + \lambda_g \left.\frac{\partial T}{\partial x}\right|_{x = x^*_{f,\mathrm{ap}}} + G_pq_{f,\mathrm{diff}} = G_pC_{p,g,p}T_f \quad (14)$$

Again, it is necessary to postulate a temperature profile in the flame to calculate the conductive term. The model incorporates a profile that is very similar to the assumed profiles in Eqs. (10) and (11):

$$T = T_f - (T_f - T_{f,\mathrm{ap}})\exp\left(-\nu\frac{x - x^*_{f,\mathrm{ap}}}{x^*_f - x^*_{f,\mathrm{ap}}}\right) \quad (15)$$

Differentiating Eq. (15) with respect to x and substituting the result into Eq. (14) gives

$$T_{f,\mathrm{ap}} = T_f - \frac{G_pq_{f,\mathrm{diff}}}{G_pC_{p,g,p} + \nu\lambda_{g,p}\big/\left(x^*_f - x^*_{f,\mathrm{ap}}\right)} \quad (16)$$

Characteristic Flame Heights

Heat transfer processes in the gas phase depend on a set of characteristic flame heights, sometimes called standoff distances. As already mentioned, the model comprises two second-order reaction flames near the surface and one diffusion flame above them.

The overall characteristic flame height x^*_f, is the sum of the characteristic heights of the reaction and diffusion flames; x^*_f and the flame temperature define the heat flux into the binder and AP flame.

The first and simplest flame is the premixed flame. It is a second-order kinetics-dominated flame that occurs directly above an oxidizer particle. The characteristic height of a one-dimensional flame of this type is[1]

$$x^*_{f,\mathrm{ap}} = G_{\mathrm{ap}}\big/\left[P^2A_{g,\mathrm{ap}}\exp(-E_{g,\mathrm{ap}}/RT_{f,\mathrm{ap}})\right] \quad (17)$$

Another second-order kinetics-dominated flame in the model is the reaction flame that occurs above the interface of the binder and oxidizer. The equation describing x^*_r is very similar to Eq. (17), with different constants. The equation is

$$x^*_r = G_p\big/\left[P^2A_r\exp(-E_r/RT_f)\right] \quad (18)$$

The diffusion flame occurs over both the reaction and premixed flames. The height of a diffusion flame is related to mass flux and a diffusion coefficient through the expression[1]

$$\frac{x^*_d \propto G_pD^{*2}}{\rho_g\mathfrak{D}} \quad (19)$$

where the diffusion coefficient $\mathfrak{D}$ has two components. The first component derives from familiar laminar mixing, which depends on the temperature, pressure, and a reference value as follows[1]:

$$\mathfrak{D}_{\mathrm{lam}} = \mathfrak{D}_0T^{1.75}\big/P \quad (20)$$

or, substituting in the ideal gas law,

$$\mathfrak{D}_{\mathrm{lam}} = \mathfrak{D}_0T^{0.75}(M_g/\Re\rho_g) \quad (21)$$

The second component derives from turbulent mixing.[10] This component depends on vorticity above the interface between the binder and oxidizer and is directly proportional to the difference between oxidizer and binder mass fluxes. Moreover, the size of the shear region above the oxidizer/binder interface is directly proportional to the characteristic oxidizer particle diameter. The turbulent mixing component is, therefore,

$$\mathfrak{D}_{\mathrm{turb}} = KD^{*2}|G_{\mathrm{ap}} - G_b|\big/\rho_g \quad (22)$$

where K is a constant of proportionality. When Eqs. (20) and (22) are substituted into Eq. (19), the total diffusional mixing height is

$$x^*_d = \frac{G_pD^{*2}}{A_{\mathrm{diff}}\left(\mathfrak{D}_0T^{0.75}_{f,\mathrm{ap}}(M_g/\Re) + KD^*|G_{\mathrm{ap}} - G_p|\right)} \quad (23)$$

where $T_{f,\mathrm{ap}}$ is a representative gas temperature for the laminar diffusion relationship and A_{diff} is a constant that converts the proportionality . Equation (22) does contain one obviously crude approximation in that it represents overall diffusivity as the simple sum of the laminar and turbulent components. The turbulent mixing component, however, only influences the model in the higher end of the pressure range in this paper (>200 bar), and so the approximation should not skew the overall results unduly.

The turbulent mixing component does add one extra calibration constant, K, and this addition can be deceptive. When calibrating the model to steady-state data, one should be cautious and minimize K so that laminar mixing dominates.

Because of the computational structure of the model, the exact values of x^*_d and x^*_r are unnecessary. Rather, their sum, $x^*_f = x^*_r + x^*_d$, is the important parameter.

Steady-State Solution

The model is a system of eight equations, Eqs. (1–3), (12), (13), and (16–18), plus Eq. (23) and eight unknowns, G_{ap}, G_b, G_p, $T_{s,\mathrm{ap}}$, $T_{s,b}$, $T_{f,\mathrm{ap}}$, $x^*_{f,\mathrm{ap}}$, and x^*_f. Four floating parameters help to calibrate the model to known steady-state data, A_{diff}, $A_{g,\mathrm{ap}}$, A_r, and K, where K should affect the model only at pressures above 200 bar. The four floating parameters do allow a lot of room for manipulation, and so

Table 1 Constants in the model[a]

Constant	Value
T_{ref}	500 K
M_g	$0.0262\,\text{J}\cdot\text{mol}^{-1}\cdot\text{K}^{-1}$
D_0	$7.585\times10^{-5}\,\text{m}^2\cdot\text{s}^{-1}$ (ref: 0 K,1 atm)
K	$1.0\,\text{m}^5\cdot\text{kg}^{-1}\cdot\text{s}^{-2}\cdot\text{K}^{-0.25}$
ν	2.5
A_r	$2\times10^{-4}\,\text{s}^3\cdot\text{kg}^{-1}\cdot\text{m}^{-1}$
$A_{g,\text{ap}}$	$2.5\times10^{-5}\,\text{s}^3\cdot\text{kg}^{-1}\cdot\text{m}^{-1}$
$A_{s,\text{ap}}$	$9.6\times10^{5}\,\text{kg}\cdot\text{s}^{-1}\cdot\text{m}^{-2}$
$A_{s,b}$	$1.225\times10^{3}\,\text{kg}\cdot\text{s}^{-1}\cdot\text{m}^{-2}$
A_{diff}	$8.0\,\text{K}^{0.25}\cdot\text{kg}\cdot\text{s}^{2}\cdot\text{m}^{-5}$
$E_{s,\text{ap}}$	$9\times10^{4}\,\text{J}\cdot\text{kg}^{-1}$
$E_{s,b}$	$3.43\times10^{4}\,\text{J}\cdot\text{kg}^{-1}$
E_r	$1.256\times10^{5}\,\text{J}\cdot\text{kg}^{-1}$
$E_{g,\text{ap}}$	$6.28\times10^{4}\,\text{J}\cdot\text{kg}^{-1}$
ρ_{ap}	$1950\,\text{kg}\cdot\text{m}^{-3}$
ρ_b	$920\,\text{kg}\cdot\text{m}^{-3}$
$q_{v,\text{ap}}$	$4.222\times10^{5}\,\text{J}\cdot\text{kg}^{-1}$
$q_{v,b}$	$-2.0\times10^{5}\,\text{J}\cdot\text{kg}^{-1}$
$C_{p,s,\text{ap}}$[b]	$1.717\cdot T+586.15\,\text{J}\cdot\text{kg}^{-1}\cdot\text{K}^{-1}$
$C_{p,s,b}$	$3.559\cdot T+1047\,\text{J}\cdot\text{kg}^{-1}\cdot\text{K}^{-1}$
$\lambda_{s,\text{ap}}$	$-3.85\times10^{-4}\cdot T+0.628\,\text{W}\cdot\text{m}^{-1}\cdot\text{K}^{-1}$
$\lambda_{s,b}$	$5.44\times10^{-5}\cdot T+0.184\,\text{W}\cdot\text{m}^{-1}\cdot\text{K}^{-1}$
$\lambda_{g,\text{ap}}$	$7.2\times10^{-5}\cdot T+0.006\,\text{W}\cdot\text{m}^{-1}\cdot\text{K}^{-1}$
$\lambda_{g,b}$	$4.33\times10^{-4}\cdot T-0.15\,\text{W}\cdot\text{m}^{-1}\cdot\text{K}^{-1}$
$\lambda_{g,p}$	$1.08\times10^{-4}\cdot T+0.0133\,\text{W}\cdot\text{m}^{-1}\cdot\text{K}^{-1}$

[a]Temperatures are in degrees Kelvin. [b]Reference 13.

Table 2 Properties that depend on O/F ratio

α_{ap}	$q_{f,\text{diff}}$, $\text{J}\cdot\text{kg}^{-1}$	T_f, K	$C_{p,g,p}$, $\text{J}\cdot\text{kg}^{-1}\cdot\text{K}^{-1}$
0.73	2.07×10^{6}	1587	2870
0.77	2.63×10^{6}	1996	2292
0.80	3.01×10^{6}	2309	2091

one should take care to keep the physical parameters in reasonable ranges when calibrating the model. As an additional complication in nonsteady simulations, the integral terms in Eqs. (12) and (13) require a calculation of the temperature profiles in the oxidizer and binder. Table 1 is a list of most of the constant properties in the model, where binder properties in this paper correspond to Isophorone diisocynate (IPDI)-cured HTPB. Although Table 1 lists solid-phase specific heat and thermal conductivity as functions of temperature, both of these properties are actually constant in the computation of the model. Specifically, $C_{p,s}(T_{\text{ref}})$ and $\lambda_s(T_{\text{ref}})$ are the values used in the computation. Gas-phase thermal conductivities are functions of flame and surface temperatures.

All of the values in Table 1 represent average values from the literature,[10–12] but three other properties, $C_{p,g,p}$, $q_{f,\text{diff}}$, and T_f, come from thermoequilibrium calculations that in turn depend on the O/F ratio. Table 2 lists these properties as a function of α_{ap}.

Steady-State Results

Figures 2 and 3 are plots of steady-state burning rate vs pressure for several types of propellants. Experimental data for 90- and 5-μm monomodal propellants with O/F ratios of 80/20 come from ultrasonic experiments done at ONERA in Palaiseau, France.[10] Data for the 200- and 17-μm propellants with O/F ratios of 75/25 come from ultrasonic experiments done at the University of Alabama at Huntsville (UAH).[13] All experimental data in Fig. 2 come from room temperature (≈295-K) tests. Error bars represent ±4% accuracy.

Figures 2 and 3 show reasonable agreement between theoretical predictions and available data. The four calibration constants, A_{diff}, K, $A_{g,\text{ap}}$, and A_r, have been adjusted to fit the ONERA data, but the theoretical cures for the 75/25 propellants are pure predictions.

Temperature sensitivity is also an important aspect of the steady-state model because it indicates the ability of the solid phase of the propellant to absorb thermal energy, which in turn plays an important role in the nonsteady response. Figure 4 shows predicted

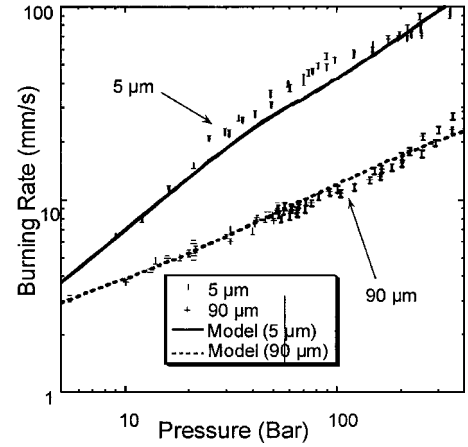

Fig. 2 Steady-state burning rates, O/F = 80/20.

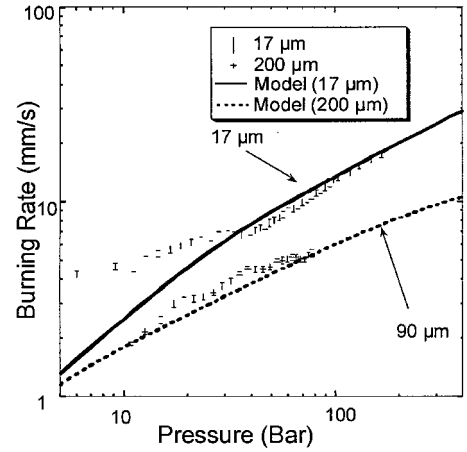

Fig. 3 Steady-state burning rates, O/F = 75/25.

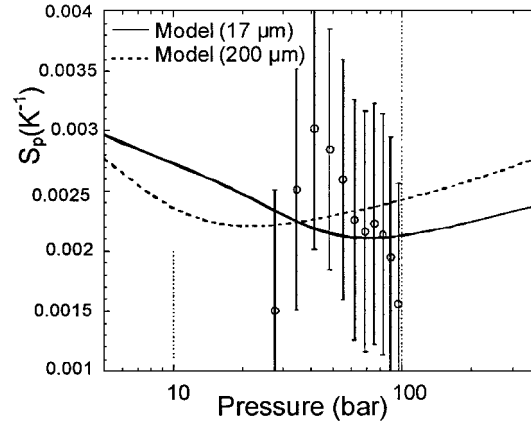

Fig. 4 Temperature sensitivity.

and experimental temperature sensitivity for the UAH propellants. All data in Fig. 4 come from calculations/tests at 20°C and 60 deg. Error bars represent a ±1°C error in temperature and a ±4% error in burning rate. Unfortunately, empirical temperature sensitivity data typically have significant scatter, as shown in Fig. 4. Nevertheless, it is encouraging to see predicted temperature sensitivities on the order of $0.003\,\text{K}^{-1}$, which is a reasonable value of σ_P for a non-aluminized AP/HTPB propellant.

Figure 5 shows theoretical surface and flame temperatures as a function of pressure for a 100-μm monomodal propellant with 80% AP and 20% HTPB. (All predictions for the remainder of this paper correspond to 298-K initial temperatures.) There does appear

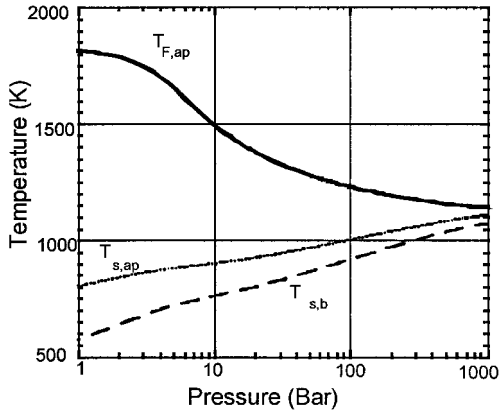

Fig. 5 Steady-state flame and surface temperatures.

to be a significant surface temperature difference between the oxidizer and binder, indicating significant lateral heat transfer. It is possible that quasi-one-dimensional models will eventually account for lateral heat transfer through a sophisticated averaging scheme, but it is more likely that future studies will need to incorporate higher dimensions to address this phenomenon properly in nonsteady simulations. Figure 5 illustrates the role of characteristic flame heights in the model. When the AP flame is very high above the surface at low pressures, its characteristic temperature is higher than the adiabatic flame temperature of pure AP (~1400 K) because the diffusion flame is feeding heat into the kinetics-dominated flames below. As the pressure rises, $x^*_{f,\mathrm{ap}}$ falls, and the heat transfer from the AP flame to the surface becomes more significant, thus lowering the characteristic temperature to a value below the adiabatic flame temperature of pure AP.

Nonsteady Solution

The integral terms in Eqs. (12) and (13) represent thermal capacitance in the solid phase of AP and binder, respectively, and thus, they drive the nonsteady response of the system. Each integral contains a $\partial T/\partial t$ term, so temperature profiles in the binder and AP at each simulation time step are necessary. The familiar transient heat conduction defines the temperature in the binder and oxidizer. It is

$$\rho C_p \frac{\partial T}{\partial t} = \frac{\partial}{\partial x}\left(\lambda \frac{\partial T}{\partial x}\right) - \rho r \frac{\partial (C_p T)}{\partial x} \tag{24}$$

where thermal properties such as C_p and λ depend on the solid substance. In the current study, thermal properties are constant in the oxidizer and likewise in the binder. Other studies have focused on the effect of temperature-dependent thermal properties and solid-phase reactions, but these studies have typically assumed a single temperature profile that results from average properties between oxidizer and binder.[5] To iterate, the current model maintains separate temperature profiles for the oxidizer and binder.

The solution of Eq. (24) is basically a simple task, except for one added difficulty: The surface temperatures and burning rates of the oxidizer and binder are unknown. They are dependent variables that must be solved iteratively with the other six dependent variables of the system. Computationally, this means that the temperature profiles in the oxidizer and binder must be resolved many times at each simulation time step until the surface temperatures match up with the other variables to form an overall solution.

One well-posed way to calculate a new temperature profile is to define it as a function of the current surface temperature and the temperature profile at the previous time step, that is,

$$\int_{-\infty}^{0} \rho_{s,\mathrm{ap}} C_{p,s,\mathrm{ap}} \left(\frac{\partial T_{\mathrm{ap}}}{\partial t}\right) \mathrm{d}x \equiv f(T_{s,\mathrm{ap,current\ iteration}}, \text{previous AP temperature profile}) \tag{25}$$

$$\int_{-\infty}^{0} \rho_{s,b} C_{p,s,b} \left(\frac{\partial T_b}{\partial t}\right) \mathrm{d}x \equiv f(T_{s,b,\mathrm{current\ iteration}}, \text{previous binder temperature profile}) \tag{26}$$

where the functions on the right-hand side of Eqs. (25) and (26) are actually numerical solutions of Eq. (24) in the oxidizer and binder, respectively.

Now that the overall computational structure is set, the actual solution, although not trivial, is not abstruse either. In steady-state calculations, any simultaneous equation algorithm, such as Newton's method, will solve the eight equations. In unsteady calculations, the same solver will work, but Eqs. (12) and (13) require the integration two temperature profiles.

The function that calculates the temperature profiles for this paper is a Crank–Nicolson finite difference scheme that accepts two boundary conditions: T_i deep within the propellant and a T_s at the surface. (T_s would correspond to a current guess value of either $T_{s,\mathrm{ap}}$ or $T_{s,b}$ at any given iteration in the main loop.) Other arguments to the function include the thermal properties, the burning rate, the time spacing, the previous temperature profile, and a vector of spatial locations that represent finite difference nodes. The function returns a new temperature profile at the next temporal step, corresponding to the T_s that was passed to it. As implied by its argument list, the function does not require a constant x spacing, and indeed for the present calculations, the x location at some point k comes from the relationship

$$x_k = (1500 \times 10^{-6}) e^{-99.88}(1 - e^{0.12k}) \tag{27}$$

The preceding spacing function decreases exponentially near the surface where temperature gradients are highest and, thus, significantly reduces the number of points necessary to resolve the temperature profile. Such computational thrift becomes important because the C++ function may potentially have to generate hundreds of temperature profiles at each simulation time step until $T_{s,\mathrm{ap}}$ and $T_{s,b}$ boundary conditions converge with the six other variables of the system.

Time-step sizes and simulation cutoff criteria depend on several factors. Two factors to consider are the characteristic response times of the system. They are

$$\tau_{\mathrm{ap}} = d_{\mathrm{ap}}/r^2_{\mathrm{ap}}, \qquad \tau_b = d_b/r^2_b \tag{28}$$

When the minimum of the minimum two values is denoted as $\tau_{\min}$ and the maximum is denoted as $\tau_{\max}$, the maximum calculation time step should, therefore, be no greater than $\tau_{\min}/19$ for the simulation to generate a reasonably sharp picture of the transient response. However, two other factors may also influence the step size. First, the time step should be no larger than $1/(37 \cdot \omega)$, where the input pressure is oscillating at frequency ω. Second, trial and error has shown that time steps larger than 10 μs can potentially lead to unacceptable error. Therefore, one can write the step size as

$$\Delta t = \min[\tau_{\min}/19,\ 1/(37\omega),\ 10\ \mu\mathrm{s}] \tag{29}$$

The overall length of the simulation similarly depends on multiple factors. The total simulation time is the greater of five pressure oscillations or $8 \cdot \tau_{\max}$.

The final task in a simulation is to calculate R_P. Figure 6 is a plot of a simulation with an oscillating pressure input. The simulation is of an propellant with an 80/20 O/F ratio and 100-μm oxidizer diameter, subjected to an input frequency of 5000 Hz. When the peaks of the mass flux during the final oscillation are considered the response magnitude for the simulation is

$$|R_P| = \frac{(G_{p,\max} - G_{p,\min})/(G_{p,\max} + G_{p,\min})}{(P_{\max} - P_{\min})/(P_{\max} + P_{\min})} \tag{30}$$

Similarly, phase shift information comes from the relationship,

$$\lfloor \mathrm{time}(\bar{G}_p) - \mathrm{time}(\bar{P}) \rfloor \cdot 2\pi\omega \tag{31}$$

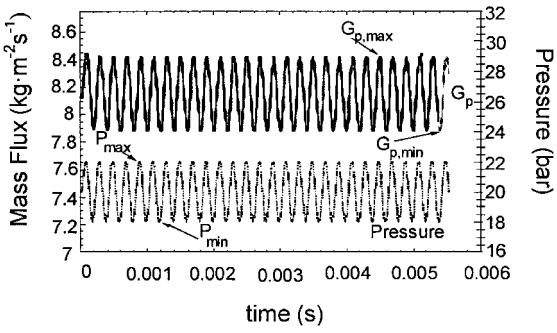

Fig. 6 Example nonsteady simulation.

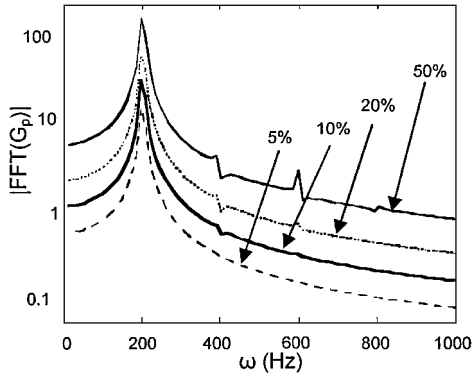

Fig. 7 FFT of mass flux at four pressure oscillation amplitudes.

where time ( ) is a function that calculates the time location of either $\bar{G}_p$ or $\bar{P}$. Most of this paper is concerned with the magnitude of the response instead of the phase, but in the following section, some representative curves will be shown.

Unfortunately, frequency-response functions are inherently linear concepts that do not apply directly to nonlinear simulations such as the one in the present study. Equations (30) and (31) are possible due to the relative "cleanness" of computer-generated data, but they are not quite correct if the simulation does not produce a sinusoidal burning rate output in response to a sinusoidal pressure input. Therefore, it is worthwhile to explore the applicability of these simplified methods to a nonlinear simulation.

Figure 7 is a plot of the Fourier spectrum of mass flux in response to a pressure input of 200 Hz. The simulation in Fig. 7 is of a propellant with 100-μm AP particle diameter, 80% AP/20% HTPB with a mean pressure of 20 bar. Each curve in Fig. 7 is the modulus of the Fourier transform of mass flux during the last few oscillations, that is, after dynamic equilibrium, at a given pressure oscillation magnitude. Input magnitudes of 20 and 50% show a distinct excitation at 200 Hz, whereas the 10% curve shows a developing nonlinearity. Figure 7 implies that pressure oscillations that are higher than 10% can induce secondary harmonics and that nonlinearity becomes significant even at relatively low-pressure oscillations. Nevertheless, the effect is not overwhelming, as shown by the scale of the abscissa of Fig. 6 compared to the maximum values.

Because R_P is such a common parameter in the literature, it is necessary to approximate it irrespective of any nonlinearity in the present study. One alternative to Eqs. (30) and (31) is to set the response function equal to the ratio of the fast Fourier transform (FFT) of the output to the FFT of the input, that is,

$$R_P = [\mathrm{FFT}(r)/\mathrm{FFT}(P)] \cdot (\bar{P}/\bar{r}) \tag{32}$$

Numerical experimentation has shown that Eq. (32) returns results that are nearly identical to that of Eqs. (30) and (31), at least in simulations with pressure oscillations smaller than 10%. Again, the fundamental problem with any method of this type is that the simulation is nonlinear, whereas the entire concept of a frequency response is inherently linear. All R_P plots for the remainder of this paper are the results of Eqs. (30) and (31).

Nonsteady Results

Figure 8 shows the effect of mean pressure on the predicted response of two propellants with an O/F ratio of 80/20. In both cases, the input oscillation magnitude is 10% of the mean pressure. One propellant has a 100-μm AP particle diameter, and the other has a 5-μm AP particle diameter. The general trend in Fig. 8 is of lowered response magnitude with increasing mean pressure. Figure 8 is not normalized by the pressure exponent, however, so that some of the effect might be due to semiplateau regions in the burning rate curves. Figure 9 is a plot of four phase shifts for the same propellants. The curves in Figure 9 show significant irregularity because the simulation temporal step size is large. Calculation of phase shifts in discrete data requires a relatively high sampling frequency, and so the simulation time step would have to be much smaller to generate smooth phase curves for example, $\frac{1}{100}\omega$.

Figure 10 shows the effect of AP particle diameter on the magnitude of the predicted response. All propellants in Fig. 10 have an

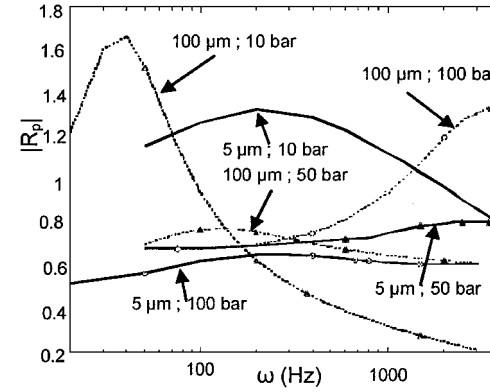

Fig. 8 Effect of mean pressure on $|R_P|$.

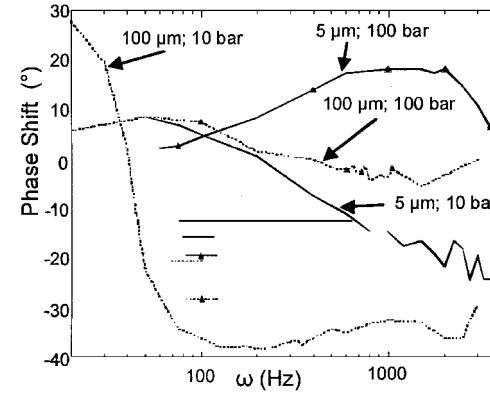

Fig. 9 Representative phase shifts.

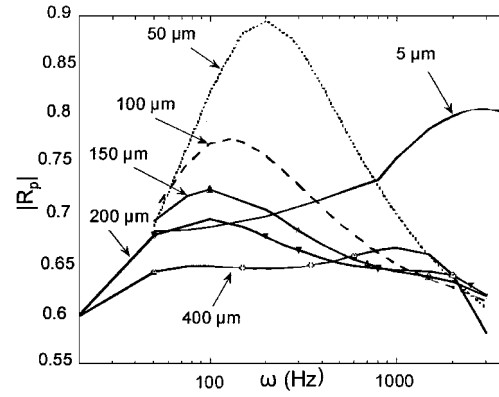

Fig. 10 Effect of oxidizer particle diameter on $|R_P|$.

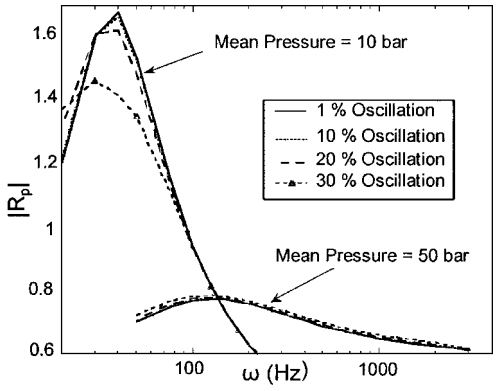

Fig. 11 Effect of input oscillation magnitude on $|R_P|$.

O/F ratio of 80/20, a mean input pressure of 50 bar, and an input oscillation magnitude of 10%. Figure 10 gives an example of how heterogeneity might affect the model. As the AP particle diameter becomes very large (>200 μm), a secondary peak appears. This peak corresponds roughly to the characteristic response time of the binder, whereas the first, lower-frequency peak corresponds to the characteristic response time of the oxidizer. Homogeneous models, that is, models that use average properties between oxidizer and binder and simpler flame structure, cannot predict this behavior.

Figure 11 shows the effect of increasing pressure oscillation magnitude. It contains two sets of curves for a 100-μm AP particle diameter propellant with an O/F ratio of 80/20. One set of curves corresponds to a mean pressure of 10 bar, and the other set of curves corresponds to a mean pressure of 50 bar.

For comparison to previous work, one can consider the effect of using average thermal properties instead of the two-profile system in the model. A propellant with a 100-μm AP particle diameter and an O/F ratio of 80/20 has a mass-averaged thermal diffusivity of 1.309×10^{-7} m$^2 \cdot$ s^{-1} and a predicted steady-state burning rate of 3.748 mm/s at a pressure of 10 bar. Thus, a model with a homogeneous solid phase would predict a maximum response magnitude at a frequency of $(0.003748 \text{ m/s})^2/(1.309 \times 10^{-7} \text{m}^2/\text{s}) = 107$ Hz. In contrast, the peak in Fig. 11 is somewhat lower. Clearly, there can be a large difference between composite propellant models that use average properties and those that consider the constituents separately.

Finally, Fig. 11 corroborates the implication of Fig. 7 that the burning rate becomes nonsinusoidal when the pressure oscillation magnitude grows larger than about 10% of the mean pressure. Above this threshold, ringing in the secondary harmonics begins to become noticeable, and the calculated $|R_P|$ starts to diverge. Figure 11 does not indicate that the magnitude of the response either increases or decreases with increasing oscillation magnitude. Rather, it indicates that the output is becoming less sinusoidal as oscillation magnitude grows larger, and thus, any method that determines $|R_P|$ assuming a sinusoidal output will have increasing error.

Conclusions

Figure 2 shows approximate agreement between experimental data and theoretical predictions, at least for pressures below about 400 bar. Temperature sensitivities are reasonable for propellants of the type being modeled.

The overall trend seems to be of a reduced response magnitude with increasing mean pressure, plus some interesting effects that come from both the heterogeneity and the nonlinearity of the present study. The heterogeneity of the model affects the response curves through two paths: shifting of the peak and development of new peaks. The primary peak in $|R_P|$ plots is still the one that is associated with the characteristic response time of the AP, but this peak, as a general rule, occurs at a somewhat lower frequency than $1/\tau_{\text{ap}}$. Moreover, when the AP particle diameter (and, thus, the diffusion flame) becomes large, the binder and AP tend to separate mechanistically, and a second peak develops near the frequency $1/\tau_b$.

Nonlinear effects are not as evident as heterogeneous effects. The first, most obvious nonlinear effect is a nonsinusoidal output in response to a sinusoidal input. This is not a significant issue for oscillation magnitudes under about 10%, as Figs. 7 and 11 indicate. The nonlinearity of the present model is certainly not useless, however, because it has the potential to predict response to nonsinusoidal pressure inputs. Such predictions should be the subject of future research.

Acknowledgments

This work was sponsored by the California Institute of Technology Multidisciplinary University Research Initiative under the Office of Naval Research Grant N00014-95-1-1338, Program Manager Judah Goldwasser. The authors would like to thank Guy Lengellé of ONERA for technical assistance and Ramon Bellec, previously of ONERA, for starting the steady-state version of the model. Edmund Rochford of the University of Alabama at Huntsville provided some of the steady-state burning rate and temperature sensitivity data. Finally, Marlow Moser and Norman Cohen provided suggestions and discussion.

References

[1]Beckstead, M., Derr, R., and Price, C., "A Model of Composite Solid-Propellant Combustion Based on Multiple Flames," *AIAA Journal*, Vol. 8, No. 12, 1970, pp. 2200–2207.

[2]King, M., "Examination of Chemical Approaches to Stabilizing Composite-Propellant Combustion," *Journal of Propulsion and Power*, Vol. 12, No. 3, 1996, pp. 554–563.

[3]Cohen, N., "Response Function Theories the Account for Size Distribution Effects: A Review," *AIAA Journal*, Vol. 19, No. 7, 1981, pp. 907–912.

[4]Galfetti, L., Riva, G., and Bruno, C., "Numerical Computations of Solid-Propellant Nonsteady Burning in Open or Confined Volumes," *Nonsteady Burning and Combustion Stability of Solid Propellants*, edited by L. De Luca, E. Price, and M. Summerfield, Vol. 143, Progress in Astronautics and Aeronautics, AIAA, Washington, DC, 1992, pp. 643–687.

[5]Louwers, J., and Gaidot, M., "Nonlinear Transient Burning of Composite Propellants: The Effect of Solid Phase Reactions," *Fourth International Symposium on Special Topics in Chemical Propulsion*, Begell House, Stockholm, Sweden, 1996, pp. 1146–1156.

[6]Cohen, N., "Review of Composite Propellant Burn Rate Modeling," *AIAA Journal*, Vol. 18, No. 3, 1980, pp. 277–293.

[7]Brewster, Q., and Son, S., "Quasi-Steady Combustion Modeling of Homogeneous Solid Propellants," *Combustion and Flame*, Vol. 103, No. 1/2, 1995, pp. 11–26.

[8]Hermance, C. E., "A Model of Solid Propellant Combustion Including Surface Heterogeneity and Heat Generation," *AIAA Journal*, Vol. 4, No. 9, 1966, pp. 1629–1637.

[9]Renie, J., Condon, J., and Osborn, J., "Oxidizer Size Distribution Effects on Propellant Combustion," *AIAA Journal*, Vol. 17, No. 8, 1979, pp. 877–883.

[10]Bellec, R., Duterque, J., and Lengellé, G., "Modeling of Aluminized Solid Propellants," ONERA, Technical Report RT 37/7128 EN, Palaiseau, France, 1996.

[11]Chen, J., and Brill, T., "Chemistry and Kinetics of Hydroxyl-terminated Polybutadiene (HTPB) and Diisocyanate-HTPB Polymers During Slow Decomposition and Combustion-like Conditions," *Combustion and Flame*, Vol. 87, 1991, pp. 217–232.

[12]Jeppson, M., Beckstead, M., and Jing, Q., "A Kinetic Model for the Premixed Combustion of a Fine AP/HTPB Composite Propellant," AIAA Paper 98-0447, Jan. 1998.

[13]Rochford, E., "Temperature Sensitivity Measurements of Solid Rocket Propellants," M.S.E. Thesis, Dept. of Mechanical and Aerospace Engineering, Univ. of Alabama in Huntsville, AL, Spring, Feb. 1999.